Surfactant-Free Aqueous Synthesis of Pure Single-Crystalline SnSe Nanosheet Clusters as Anode for High Energy- and Power-Density Sodium-Ion Batteries

Shuang Yuan, Yun-Hai Zhu, Wang Li, Sai Wang, Dan Xu, Lin Li, Yu Zhang, and Xin-Bo Zhang**

Tin selenide (SnSe), as an important member of layered metal chalcogenides, shows great promises for important applications including thermoelectric devices, solar cells, energy storage, etc.[1] However, despite significant progresses have been achieved in SnSe synthesis, most methods still highly rely on toxic, expensive and air-sensitive Se precursors such as trioctylphosphine selenide and bis(trimethylsilyl)selenide, which intrinsically limit its large-scale application.[2] Even so, as the Sn (II) is prone to be oxidized to Sn (IV), thus controlling the composition or phase to obtain pure SnSe becomes very challenging. As a result, pure single-crystalline SnSe nanosheet has not been synthesized using environmental friendly and low-cost precursors in aqueous condition, to say nothing with 3D hierarchical nanostructure. Therefore, developing a facile approach for chemical composition- and shape-controlled synthesis of hierarchically nanostructured SnSe is highly desirable for both fundamental studies and practical applications.

High power- and energy-density electrochemical energy storage devices are becoming increasingly important.[3] Due to the fact that Na resources are practically inexhaustible and ubiquitous, room-temperature Na-ion batteries (NIBs) have again aroused intensive interest as an important alternative to lithium-ion batteries (LIBs).[4] However, since Na ion is larger and heavier than Li ion, achieving high power- and energy-density thus become even more difficult than that of LIBs.[5] Some promising anode materials of LIBs are actually found to be plagued by low capacity, inferior rate capability, or even complete electrochemical inactivity in NIBs.[6] Due to the high theoretical capacity and abundant resource, SnSe could be a promising anode material for NIBs. However, the low electrical conductivity, slow solid-state diffusion of Na ions, and instability of solid electrolyte interphase caused by repetitive volume expansion and contraction inevitably result in serious kinetic problems, which make it difficult to fully utilize the conversion reactions, and result in limited capacity and rate capabilities in practice.[7a-c] In response, construction of SnSe with 3D hierarchical nanostructure composed of interconnected thin single-crystal SnSe nanosheet could potentially solve this problem due to the salient feature of shorter diffusion length and higher electrode/electrolyte contact area as well mechanical stability compared to isolated thin nanosheet. Thereafter, developing new strategy to synthesize pure single-crystalline SnSe nanosheet clusters (SnSe NSCs) and then exploring its electrochemical performance toward sodium is urgently desirable but remains a great challenge.

Herein, we first develop and demonstrate a cost- and time-effective surfactant-free aqueous solution strategy for the phase-controlled synthesis of SnSe NSCs, wherein low cost, air stable, and environmental friendly commercial bulk Se powder is used as Se precursor and the reaction time is less than 300 s. Unexpectedly, the obtained SnSe NSCs exhibit superior electrochemical performances as anode materials for NIBs, including high capacity (738 mAh g^{-1}) and particularly superior rate capability even at 40 A g^{-1}. Furthermore, a high discharge voltage platform of ≈3.4 V and high energy density up to 141 Wh kg^{-1} are obtained in full cell. The above-mentioned electrochemical performance of SnSe NSCs has manifested its promising application in NIBs, which greatly expands the range of anode choices of NIBs.

The low-magnification transmission electron microscopy (TEM) image and scanning electron microscopy (SEM) image (**Figure 1**a and Figure S1, Supporting Information) show that the obtained sample holds a 3D hierarchical nanostructure, which are assembled by interconnected thin nanosheets with a width up to several hundred nanometers and a thickness of ≈36.6 nm (atomic force microscopy (AFM), Figure 1b). Their porous structure is further confirmed by the nitrogen (N_2) absorption–desorption isotherms (Figure S2, Supporting Information). In addition, high-resolution TEM and selected area electron diffraction (SAED) (Figure 1c and inset, Figures S3, S4, Supporting Information) reveal the high purity and single crystalline nature of the thin nanosheets with lattice

Dr. S. Yuan, Y.-H. Zhu, S. Wang, Dr. D. Xu, L. Li, Prof. X.-B. Zhang
State Key Laboratory of Rare Earth Resource Utilization
Changchun Institute of Applied Chemistry
Chinese Academy of Sciences
Changchun 130022, China
E-mail: xbzhang@ciac.ac.cn
Dr. S. Yuan, Y.-H. Zhu, S. Wang
Key Laboratory of Automobile Materials
Ministry of Education and College of Materials Science and Engineering
Jilin University
Changchun, 130012 Jilin, China
W. Li, Prof. Y. Zhang
Key Laboratory of Bio-Inspired Smart Interfacial Science and Technology of Ministry of Education
School of Chemistry and Environment
Beihang University
Beijing 100191, P. R. China
E-mail: jade@buaa.edu.cn

DOI: 10.1002/adma.201602469

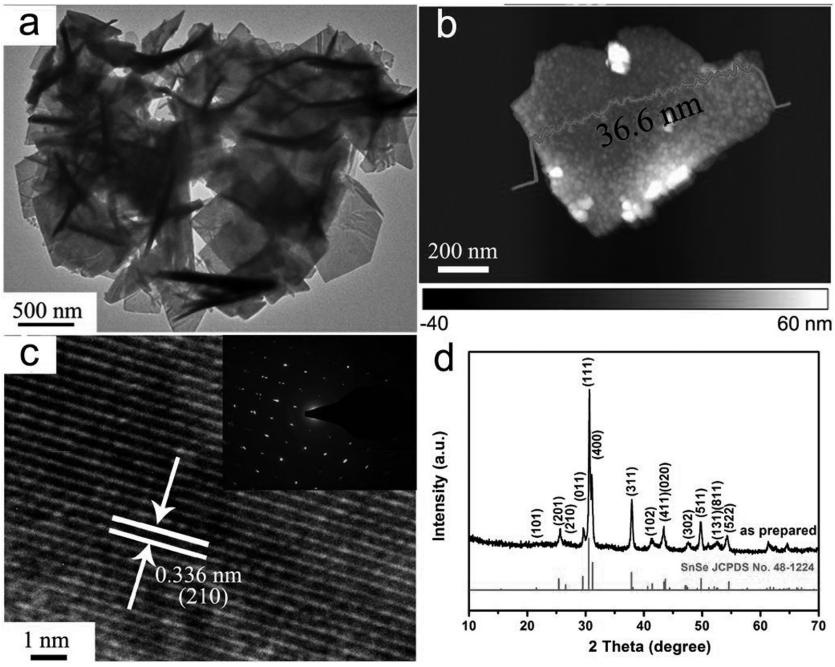

Figure 1. a) TEM image, b) AFM images, c) HRTEM (inset: SAED), and d) XRD patterns of SnSe NSCs.

distance of 0.336, 0.28, 0.29, 0.30, and 0.41 nm, which are well-matched to (210), (400), (111), (011), and (101) planes of SnSe. Additionally, its high purity is confirmed by the X-ray diffraction (XRD) result (Figure 1d), wherein all the diffraction peaks can be well indexed to orthorhombic SnSe phase (JCPDS: 48-1224). X-ray photoelectron spectroscopy (XPS) spectra in Figure S5 (Supporting Information) further confirmed the high purity of the obtained SnSe. The favorable combination of hierarchical nanostructure and highly pure single-crystal structure of SnSe NSCs would facilitate the dispersion and diffusion of electrolyte and electron, respectively, and thus benefit the electrochemical performance, especially rate capability (vide infra).

To clearly figure out the mechanism of the rapid formation of SnSe NSCs, their growth process was tracked by their morphology variation. Before reaction, the commercial Se powder holds bulk morphology (**Figure 2**a). Upon dropped to 10 M NaOH solution, it dissolves and forms Se_x^{2-} via a disproportionation and subsequent coordination reactions (reaction 1: $3Se + 6OH^- \rightarrow 2Se^{2-} + SeO_3^{2-} + 3H_2O$; reaction 2: $Se^{2-} + (x-1)\,Se \rightarrow Se_x^{2-}$; Figure 2d). Then, after citric acid added into Sn^{2+} solution, SnSe nanoparticles (NPs) are formed rapidly (reaction 3: $Sn^{2+} + xSe^{2-} \rightarrow SnSe + (x-1)\,Se$; Figure 2b,e). Finally, SnSe NPs are further assembled into 3D hierarchical structure (Figure 2c,f), which might be attributed to an Ostwald ripening process. Interestingly, it is found that the OH^- environment plays a key role for the purity and morphology of SnSe (Figure S6, S7, Supporting Information). In sharp contrast, when Se_x^{2-} solution with OH^- is dropped into Sn^{2+} solution with citric acid (CA), only mixture of SnSe and Se powder can be obtained, which might be due to the fact that alkaline environment is necessary to facilitate the forward reaction (reaction 1) to maintain enough concentration of Se_x^{2-} and/or avoid the side reaction toward the formation of Se ($SeO_3^{2-} + Se_x^{2-} + xSn^{2+} + 6H^+ \rightarrow xSnSe + Se + 3H_2O$). It is surprising that the well-crystalline SnSe can be efficiently obtained in less than 60 s (Figure S8, Supporting Information), and the proposed preliminary reaction mechanism is schematically illustrated in Figure 2g. Herein, we also investigated the morphology and purity of SnSe by adjust the OH^- concentration (5/10/15/20 M) using different alkali sources (LiOH/NaOH/KOH). It is found that the purity and morphology of the SnSe are different. As shown in Figures S9 to S19 (Supporting Information), the species and concentration of alkali have great effect on morphology and purity of SnSe. Investigations toward detailed growth mechanism of SnSe are still in progress.

Coin cells with a metallic sodium anode are then assembled to investigate the electrochemical performance of the SnSe NSCs at 25 °C. **Figure 3**a shows the comparison of the galvanostatic discharge/charge profiles of SnSe NSCs and SnSe particles electrodes. Interestingly, the SnSe NSCs exerts very high reversible capacity of 738 mAh g^{-1} at a current density of 25 mA g^{-1}, which is more than 94% of its theoretical capacity (780 mAh g^{-1}) and among the anode materials of NIBs with highest capacity. In sharp contrast, although with similar particle size (Figure S10, Supporting Information), the SnSe particles only exhibits a much lower capacity of 495 mAh g^{-1}, indicating the superiority of 3D hierarchical nanostructure for maximizing the usage of the conversion reactions of SnSe. In addition, the discharge/charge profiles of SnSe NSCs show small polarization, indicating a low electrode resistance, which is very beneficial for achieving high power density.[8] After 30 cycles, the discharge capacity of SnSe NSCs is 730 mAh g^{-1}, it is much higher than that of SnSe particles 332 mAh g^{-1} (Figure S20, Supporting Information). Figure 3b demonstrates the rate capacity of these electrodes at current densities from 0.1 to 40 A g^{-1}. Unexpectedly, even at very high discharge/charge current densities of 10/20/30/40 A g^{-1} (≈60/180/720/2400C, a rate of n C corresponds to a full discharge in $1/n$ h), the SnSe NSCs electrode can still deliver 200/106/32/16 mAh g^{-1} discharge capacity, respectively, which are much higher than SnSe particles (81/0.19/0/0 mAh g^{-1}). To the best of our knowledge, this is the first time that such excellent rate capability has been successfully achieved without the help of high content conductive carbon additive (Table S1, Supporting Information). Furthermore, both SnSe NSCs and SnSe NPs electrodes can exhibit high capacity when the current density decrease to 50 mA g^{-1} even after the rate capability test at current density of 40 A g^{-1}, which might indicate the high stability of the formed solid electrolyte interface (SEI) on the electrode surface.[7,8a,9]

Inspired by the excellent rate capability of SnSe NSCs, from the viewpoint of practical application, we then test the cycling stability under high discharge/charge current densities. As shown in Figure 3c, the SnSe NSCs electrodes can also exhibit stable capacity of 271, 183, 70 mAh g^{-1} at the current densities

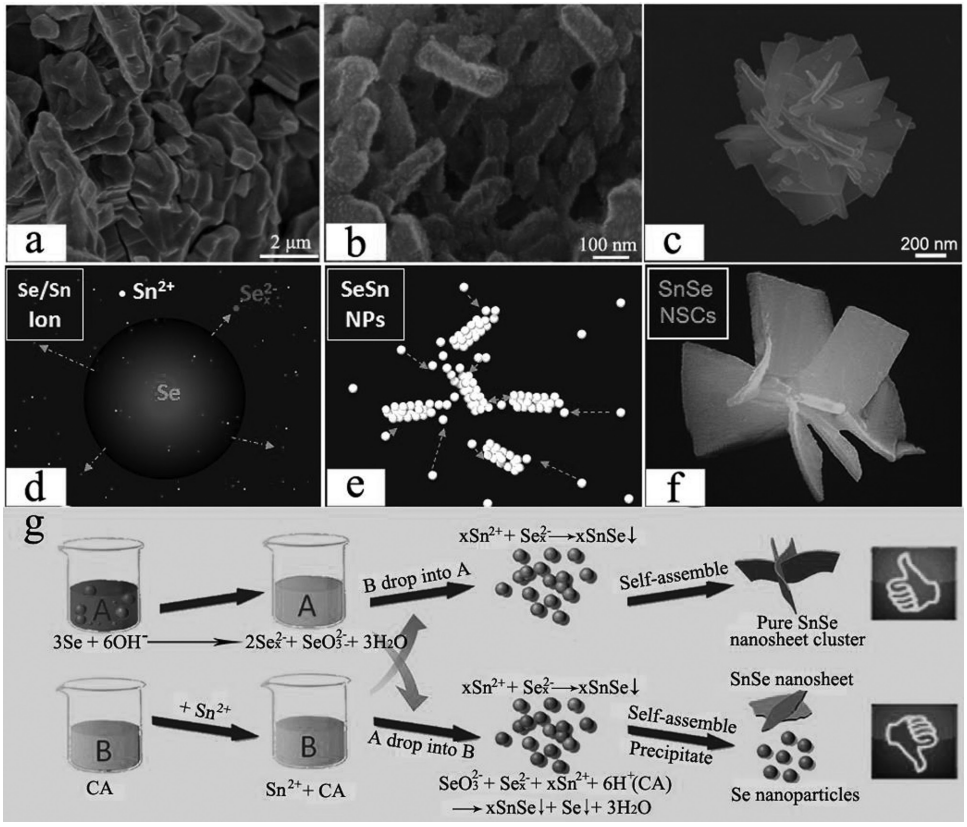

Figure 2. a–c) SEM images of bulk Se powder before, during and after reaction, d–g) schematically illustrates the procedure for the preparation of SnSe NSCs.

of 0.2/2.0/5.0 A g^{-1} (≈3/6/20C) even after 100 cycles, respectively, these performances are much higher than that of SnSe particles electrodes (Figure S21, Supporting Information). In addition, the coulombic efficiency is nearly 100% at a current density of 2.0 A g^{-1}, showing that the stable SEI and fast electron/ion pathway are formed using nanosheet structure and fluorinated ethylene carbonate (FEC) as electrolyte additive. The cycling stability of SnSe NSCs is also shown in Figure S22 (Supporting Information) to confirm the advantage of adding FEC in the electrolyte. As shown in Figure S22 (Supporting Information), the capacity of SnSe NSCs seriously decreased after 50 cycles when using FEC-free electrolyte. In addition, the impedance resistance of the SnSe NSCs with FEC, SnSe NSCs without FEC, and SnSe particle with FEC electrodes after different charge cycles are shown in Figure S23 (Supporting Information) to further demonstrate the advantages of FEC additive and nanosheet structure of SnSe NSCs. Moreover, the SEI and charge transfer resistances of these three kinds of electrode are also displayed in Figure S24 (Supporting Information). The galvanostatic intermittent titration technique (GITT) performance plots also demonstrate fast Na^+ diffusion in SnSe NSCs electrode (Figure S25, Supporting Information). Furthermore, SnSe NSCs electrodes can also operate at 0 °C (Figure S26, Supporting Information) and 10 °C (Figure S27, Supporting Information). The electrochemical performances of SnSe NSCs electrodes using $NaClO_4$/PC electrolyte with and without FEC at 25 °C are also shown in Figures S28,S29 (Supporting Information). All of these results provide definite evidence that SnSe NSCs is able to work in a lower temperature and can also work in different electrolyte. Additionally, FEC can help stabilize SEI film and the nanosheet structure is also crucial for improving battery stability.

To understand the above obtained superior electrochemical performances, reactions and phase variation of SnSe NSCs upon Na insertion/extraction are investigated by cyclic voltammetry (CV) and ex situ XRD techniques. As depicts in **Figure 4**a, the CV curves of SnSe NSCs between 0 and 3.0 V show that, during the first discharge process, the SEI and Na_xSe film are generated at ≈0.62 V,[10a] The desodiation process presents several peaks positioned at 0.13, 0.38, and 0.75 V, which might be derived from the $Na_{15}Sn_4$, Na_9Sn_4, and $NaSn_5$ generated during the discharge process, respectively.[10b] The cathodic/anodic couples located at 0.64/1.22, 0.76/1.42, and 0.92/1.67 V might be assigned to the redox reactions between Na_xSe and Na^+.[10a,11] The cathodic peak centered at 0.62 V in the first cycle shift to higher potential in subsequent cycles, which might be partially attributed to the improvement of the electronic conductivity of the electrode after the first cycle. The stable anodic and cathodic peaks after the first cycle demonstrate good cycling stability of the SEI and SnSe. To investigate the phase evolution of SnSe upon Na^+ insertion/extraction, we conduct ex situ XRD measurement on the SnSe NSCs electrodes at different states (Figure 4b), wherein the states are corresponding to the points 1 to 7 in Figure 4a. When discharge to 0.37 V (just before

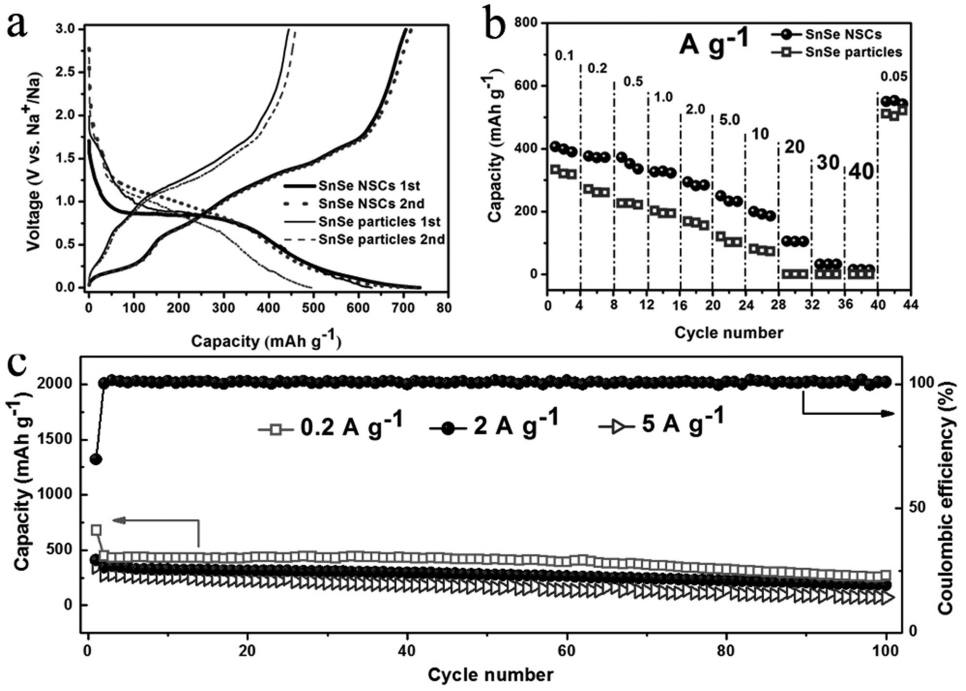

Figure 3. a) Galvanostatic discharge/charge profiles of SnSe NSCs at current density of 25 mA g^{-1}. b) Rate capability of SnSe NSCs and SnSe particles electrodes at various current densities from 0.1 to 40 A g^{-1}. c) Coulombic efficiency of SnSe NSCs at 2.0 A g^{-1} and cycling stability of SnSe NSCs at 0.2/2.0/5.0 A g^{-1}.

sodiation of Sn,[10b] point 3) and 0 V (point 4), all the peaks of SnSe NSCs disappear gradually, indicating that the generated Na_2Se compounds are amorphous. In addition, the TEM and EDS elemental mapping images (Figure S30, Supporting Information) show that small $Na_{15}Sn_4$ nanoparticles are uniformly dispersed in amorphous Na_2Se matrix after discharge to 0 V, which support the above XRD results.[12a] From points 5 to 7, some of SnSe peaks recover gradually, indicating the formation of SnSe during charging process. The weak intensity of the SnSe peaks shows that the formed SnSe particles are very small in size (Figures S31a, 32b, Supporting Information), which would benefit the kinetic of subsequent Na^+ insertion/extraction reaction.[7a,12a] It should be noted that the remained Na–Sn alloy nanoparticles in the electrode after charging process in situ form a conductive matrix (Figure S31c–32f, Supporting Information) with intimate contract with the active component, which should be responsible for the above obtained superior electrochemical performances especially the rate capability.[12] This mechanism is further supported by XPS spectra in Figure S32 (Supporting Information).

Encouraged by the superior half cells performance, to pave the way for practical application, we then assemble full cells using SnSe NSCs and $Na_{0.67}Ni_{0.41}Mn_{0.72}O_2$ (NNMO) as anode and cathode materials, respectively. The SEM image and charge/discharge profiles of NNMO are shown in Figure S33 (Supporting Information). Interestingly, these full cells show a very high average discharge voltage of ≈3.4 V and a high initial capacity of 177 μAh at a current of 30 μA, corresponding to a

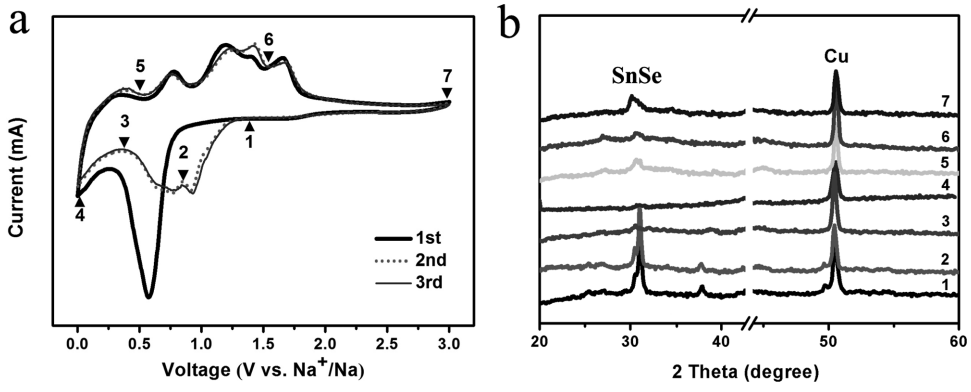

Figure 4. a) CV profiles of SnSe NSCs. b) Ex situ XRD patterns of SnSe NSCs at different charge/discharge states.

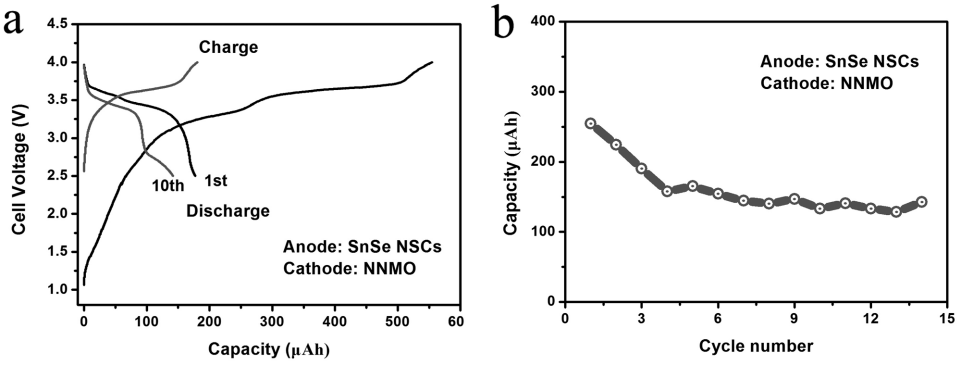

Figure 5. a) Galvanostatic discharge/charge profiles of the SnSe NSCs/NNMO full cell at 30 μA. b) Cycling performance of the full cell at 50 μA.

high energy density of 141 Wh kg^{-1}. In addition, there is still a 142 μAh capacity retained after ten cycles (**Figure 5**a). Furthermore, when cycled at 50 μA, the capacity still reaches 143 μAh after 15 cycles (Figure 5b). It should be noted that, even without optimization of battery assembly parameters, these obtained electrochemical performances are comparable or even exceeds some of the reported LIB systems (Table S2, Supporting Information), showing the great promise of SnSe NSCs as anode materials for next generation NIBs. Surprisingly, SnSe NSCs can also be employed supercapacitor electrode materials (Figure S34, Supporting Information).

The above-obtained superior electrochemical performances of SnSe NSCs, especially the ultrafast discharge/charge capability and high energy density, have rarely been reported, which are considered to be attributed to the following favorable advantages of SnSe NSCs: (i) the 3D hierarchical NSCs architecture can simultaneously improve the essential reaction interphases for the fundamental energy storage processes—it can facilitate the diffusion of electrolyte ions and transport of electrons, thus allowing the electrochemical activity of SnSe to be efficiently utilized and accommodates the volume variation during the Na uptake and release process.[7,8,13] Figure S35a–d (Supporting Information) show the SEM images of SnSe with nanosheet and particle morphology after different cycles. Even after 10 cycles, the electrode of SnSe NSCs can still keep a porous structure composed of well-distributed SnSe nanoparticles, which could facilitate the diffusion of electrolyte and Na ion inside the electrode and each SnSe nanoparticles, respectively, and then improve the electrochemical performances. In sharp contrast, for SnSe particle electrode, only after 10 cycles, the SnSe particles are aggregated and seriously degrade the porosity of the electrode, which should be responsible for the poor electrochemical performance; (ii) during discharge/charge process, lots of alloy nanoparticles are dispersed within Na_2Se matrix owing to the nanometric nature of this composite. Such reactions are shown to be highly reversible, providing outstanding capacities to store Na;[7a,12] (iii) The electrolyte additive FEC played an extremely important role during the formation of SEI, which prevents not only the decomposition of electrolyte, but also oxidation of the active materials. Surprisingly, FEC significantly not only decrease of both SEI and charge-transfer resistances of the electrode but also improve their stability upon cycling. Furthermore, even with FEC, SEI and charge-transfer resistances of electrode with SnSe nanosheet clusters are much smaller than these of electrode with SnSe particles.

In summary, pure single-crystalline SnSe NSCs are first prepared by a surfactant-free aqueous solution strategy in less than 300 s, wherein low cost, air stable, and environmental friendly commercial bulk Se powder is used as a Se precursor. Unexpectedly, as a proof-of-concept application, the obtained 3D hierarchical SnSe NSCs exhibit superior electrochemical performances as anode materials for NIBs including high reversible capacity of 738 mAh g^{-1}, good cycle stability and especially excellent ultrahigh rate capability even at 40 A g^{-1}, which are superior over its SnSe particles counterpart and most reported NIBs anode, demonstrating the significance of controlling the purity, morphology of SnSe and the SEI in improving NIBs' capacity and rate capability. Furthermore, even without optimization, the SnSe NSCs show a very high discharge voltage platform (3.4 V) and high energy density (141 Wh kg^{-1}) in metallic sodium-free full cells. The obtained promising electrochemical results and scientific understanding show great promise of SnSe NSCs and would provide design principle and encourage more research for other high-performance electrode for next-generation NIBs.

Supporting Information

Supporting Information is available from the Wiley Online Library or from the author.

Acknowledgements

This work was financially supported by 100 Talents Program of the Chinese Academy of Sciences, and National Program on Key Basic Research Project of China (2012CB215500 and 2014CB932300).

Received: May 9, 2016
Revised: July 11, 2016
Published online: November 22, 2016

[1] a) X. Liu, Y. Li, B. Zhou, X. Wang, A. N. Cartwright, M. T. Swihar, *Chem. Mater.* **2014**, *26*, 3515; b) L. D. Zhao, S. Lo, Y. Zhang, H. Sun, G. Tan, C. Uher, C. Wolverton, V. P. Dravid, M. G. Kanatzidis, *Nature* **2014**, *508*, 373; c) S. Liu, X. Guo, M. Li, W. Zhang, X. Liu, C. Li, *Angew. Chem. Int. Ed.* **2011**, *50*, 1.

[2] a) C. Zhang, H. Yin, M. Han, Z. Dai, H. Pang, Y. Zheng, Y. Lan, J. Bao, J. M. Zhu, *ACS Nano* **2014**, *8*, 3761; b) L. Li, Z. Chen, Y. Hu, X. Wang, T. Zhang, W. Chen, Q. B. Wang, *J. Am. Chem. Soc.* **2013**, *135*, 1213; c) J. Ning, G. Xiao, T. Jiang, L. Wang, Q. Dai, B. Zou, B. Liu, Y. Wei, G. Chen, G. T. Zou, *CrystEngComm* **2011**, *13*, 4161.

[3] a) Q. F. Zhang, E. Uchaker, S. L. Candelaria, G. Z. Cao, *Chem. Soc. Rev.* **2013**, *42*, 3127; b) J. J. Wang, Y. L. Li, X. L. Sun, *Nano Energy* **2013**, *2*, 443; c) J. S. Wu, X. H. Rui, C. Y. Wang, W. B. Pei, R. Lau, Q. Y. Yan, Q. C. Zhang, *Adv. Energy Mater.* **2015**, 1402189.

[4] a) M. V. Reddy, G. V. Subba Rao, B. V. R. Chowdari, *Chem. Rev.* **2013**, *113*, 5364; b) Y. Yu, L. Gu, C. Zhu, P. A. van Aken, J. Maier, *J. Am. Chem. Soc.* **2009**, *131*, 15984; c) Y. Sun, L. Zhao, H. Pan, X. Lu, L. Gu, Y. S. Hu, H. Li, M. Armand, Y. Ikuhara, L. Q. Chen, X. J. Huang, *Nat. Commun.* **2013**, *4*, 1870; d) Y. U. Park, D. H. Seo, H. S. Kwon, B. Kim, J. Kim, H. Kim, I. Kim, H. Yoo, K. Kang, *J. Am. Chem. Soc.* **2013**, *135*, 13870.

[5] a) J. F. Qian, Y. Xiong, Y. L. Cao, X. Ai, H. X. Yang, *Nano Lett.* **2014**, *14*, 1865; b) S. W. Wang, L. J. Wang, Z. Q. Zhu, Z. Hu, Q. Zhao, J. Chen, *Angew. Chem. Int. Ed.* **2014**, *53*, 5892; c) K. H. Ha, S. H. Woo, D. Mok, N. S. Choi, Y. Park, S. M. Oh, Y. Kim, J. Kim, J. Lee, L. F. Nazar, K. T. Lee, *Adv. Energy Mater.* **2013**, *3*, 770.

[6] a) H. L. Pan, Y. S. Hu, L. Q. Chen, *Energy Environ. Sci.* **2013**, *6*, 2338; b) K. Saravanan, C. W. Mason, A. Rudola, K. H. Wong, P. Balaya, *Adv. Energy Mater.* **2012**, *3*, 444; c) Z. H. Nie, D. Fava, E. Kumacheva, S. Zou, G. C. Walker, M. Rubinstein, *Nat. Mater.* **2007**, *6*, 609; d) D. Su, G. X. Wang, *ACS Nano* **2013**, *7*, 11218.

[7] a) P. G. Bruce, B. Scrosati, J. M. Tarascon, *Angew. Chem. Int. Ed.* **2008**, *47*, 2930; b) J. Jiang, Y. Li, J. Liu, X. Huang, C. Yuan, X. W. Lou, *Adv. Mater.* **2012**, *24*, 5166; c) K. T. Lee, J. Cho, *Nano Today* **2011**, *6*, 28.

[8] a) X. Huang, H. Yu, J. Chen, Z. Lu, R. Yazami, H. H. Hng, *Adv. Mater.* **2014**, *26*, 1296; b) J. Haag, G. Pattanaik, M. F. Durstock, *Adv. Mater.* **2013**, *25*, 3238; c) Y. Kim, Y Kim, A. Choi, Sangwon Woo, D. Mok, N. Choi, Y. Jung, J. Ryu, S. M. Oh, K. T. Lee, *Adv. Mater.* **2014**, *26*, 4139.

[9] a) H. Nakai, T. Kubota, A. Kita, A. Kawashima, *J. Electrochem. Soc.* **2011**, *158*, A798; b) A. Darwiche, C. Marino, M. T. Sougrati, B. Fraisse, L. Stievano, L. Monconduit, *J. Am. Chem. Soc.* **2012**, *134*, 20805; c) J. Qian, X. Wu, Y. Cao, X. Ai, H. X. Yang, *Angew. Chem. Int. Ed.* **2013**, *52*, 4633; d) Y. Kim, Y. Par, A. Choi, N. Choi, J. Kim, J. Lee, J. Ryu, S. M. Oh, K. T. Lee, *Adv. Mater.* **2014**, *26*, 4037.

[10] a) C. Luo, Y. Xu, Y. Zhu, Y. Liu, S. Zheng, Y. Liu, A. Langrock, C. S. Wang, *ACS Nano* **2013**, *7*, 8003; b) L. D. Ellis, T. D. Hatchard, M. N. Obrovac, *J. Electrochem. Soc.* **2012**, *159*, A1801.

[11] H. L. Zhu, Z. Jia, Y. Chen, N. Weadock, J. Wan, O. Vaaland, X. Han, T. Li, L. B. Hu, *Nano Lett.* **2013**, *13*, 3093.

[12] a) Y. Kim, Y. Kim, Y. Park, Y. N. Jo, Y. J. Kim, N. S. Choi, K. T. Lee, *Chem. Commun.* **2015**, *51*, 50; b) K. Kirshenbaum, D. C. Bock, C. Y. Lee, Z. Zhong, K. J. Takeuchi, A. C. Marschilok, E. S. Takeuchi, *Science* **2015**, *9*, 149.

[13] a) J. Y. Liao, A. Manthiram, *Adv. Energy Mater.* **2014**, *4*, 1400403; b) J. H. Pikul, H. G. Zhang, J. Cho, P. V. Braun, W. P. King, *Nat. Commun.* **2013**, *4*, 173.